

Convenient adhesive strength evaluation method in terms of the intensity of singular stress field

Nao-Aki NODA^{*,‡}, Rong LI^{*}, Tatsujiro MIYAZAKI[†], Rei TAKAKI^{*} and Yoshikazu SANO^{*}

^{*} Department of Mechanical Engineering, Kyushu Institute of Technology,
1-1 Sensui-cho Tobata-ku, Kitakyushu-shi 804-8550, Japan

[†] Department of Mechanical Systems Engineering, University of the Ryukyus,
1 Senbaru, Nishihara-cho, Nakagami-gun, Okinawa 903-0213, Japan

[‡]noda@mech.kyutech.ac.jp

Received (Day Month Year)

Revised (Day Month Year)

A convenient evaluation method is proposed for the debonding adhesive strength in terms of the intensity of singular stress field (ISSF) appearing at the end of interface. The same FEM mesh pattern is applied to unknown problems and reference problems. It is found that the ISSF is obtained accurately by focusing on the FEM stress at the adhesive corner. Then, the debonding condition can be expressed as a constant value of critical ISSF. The usefulness of the present solution is verified by comparing with the results of the conventional method.

Keywords: Intensity of singular stress field; Strength evaluation; Fracture mechanics; Adhesively bonded joints.

Nomenclature

Symbols

E	Young's modulus
F_σ	Dimensionless ISSF
G	Shear modulus
h	Adhesive thickness
K_σ, K_t	ISSF
$K_{\sigma c}$	Critical ISSF
l_1	Adherend length of single lap joint
l_{ad}	Adhesive length of single lap joint
P_{of}	Experimental fracture load
t_1	Adherend thickness of single lap joint
t_{ad}	Adhesive thickness of single lap joint
r	Radial distance away from the singular point
w	Width of the bonded strip
$f_{\theta\theta}(\theta, \lambda_k), f_{r\theta}(\theta, \lambda_k)$	Non-dimensional functions of angle θ and λ_k
α, β	Dundurs' material composite parameters
θ	Angle from the interface corner
λ	Singular index
σ_y, τ_{xy}	Tension and shear stress component near the crack tip
σ_o	Tension at both ends of single lap joint
σ_c	Adhesive tensile strength

[‡] Corresponding author

τ_c	Average shear stress at fracture
$\sigma_y^{FEM*}, \tau_{xy}^{FEM*}$	FEM stresses at the interface corner of the reference problem
$\sigma_y^{FEM}, \tau_{xy}^{FEM}$	FEM stresses at the interface corner of the given unknown problem
ν	Poisson's ratio
<i>Abbreviations</i>	
FEM	Finite element method
ISSF	Intensity of singular stress field
RWCIM	Reciprocal work contour integral method

1. Introduction

Due to their low cost and high performance, adhesive joints are widely used in a variety of industries [Cheng *et al.* (2015); Barnes and Pashby (2000)]. For example, IC/LSI packages contain various interfaces for the connection of the semiconductor to the substrate, resin seal of semiconductor and multilayer structure. Therefore, in order to ensure the reliability of the packages of semiconductors, the proper method is required for evaluating the debonding strength [Shibutani (2004); Hattori *et al.* (1988); Shiratori (1994); Takahashi *et al.* (2016); Hirata *et al.* (2006)]. Generally, the debonding strength of the dissimilar joints depends on the material combination, load condition, adhesive condition and so on. Since the experimental evaluation is time-consuming, the practical and convenient analysis with a debonding fracture criterion is desirable. Several adhesive strength evaluations have been done analytically [Khan *et al.* (2017); Pathak *et al.* (2017); Gautam and Sauer (2014)].

The increasing use of adhesive joints has generated a lot of interest in understanding the stress and crack initiation in the adhesive. Since the singular stress field usually exists at the interface end [Bogy (1968); Bogy (1971); Yuuki (1993); Treifi and Oyadiji (2013)], the interfacial debonding often occurs under thermal and mechanical loading [Hattori *et al.* (1988)]. In the previous studies [Mintzas and Nowell (2012); Qian and Akisanya (1998); Reedy (1993)], the adhesive strength was predicted in terms of the intensity of the singular stress field (ISSF) used as the debonding criterion. Recently, the authors have proposed a mesh independent technique to calculate ISSFs [Zhang *et al.* (2010); Zhang *et al.* (2015)]. Then, the authors have shown that the adhesive strength can be expressed as a constant value of critical ISSF ($K_{\sigma_c} = \text{const.}$) for both brittle and ductile adhesive butt joints as shown in Fig. 1 [Noda *et al.* (2015)].

The single-lap shear testing [BS EN 1465 (1995); ASTM D 1002-1 (2003)] is a general testing method widely used. In this study, therefore, the debonding condition of the single lap joint specimens in Fig.2 [Park *et al.* (2010)] will be discussed by focusing on ISSF. In Section 2, the mesh-independent technique proposed previously will be outlined by taking an example of 2D butt joint. In Section 3, a convenient evaluation method will be proposed for the single lap joint by focusing on the ISSF. In Section 4, the ISSF for the SLJ [Park *et al.* (2010)] will be analyzed by changing the adherend and adhesive geometries. Finally, in Section 5, a convenient method will be proposed to

evaluate the adhesive strength since the previous debonding fracture criteria were not very simple and convenient [Nono and Nagahiro (1986); Kyogoku *et al.* (1986); Rodríguez *et al.* (2012)].

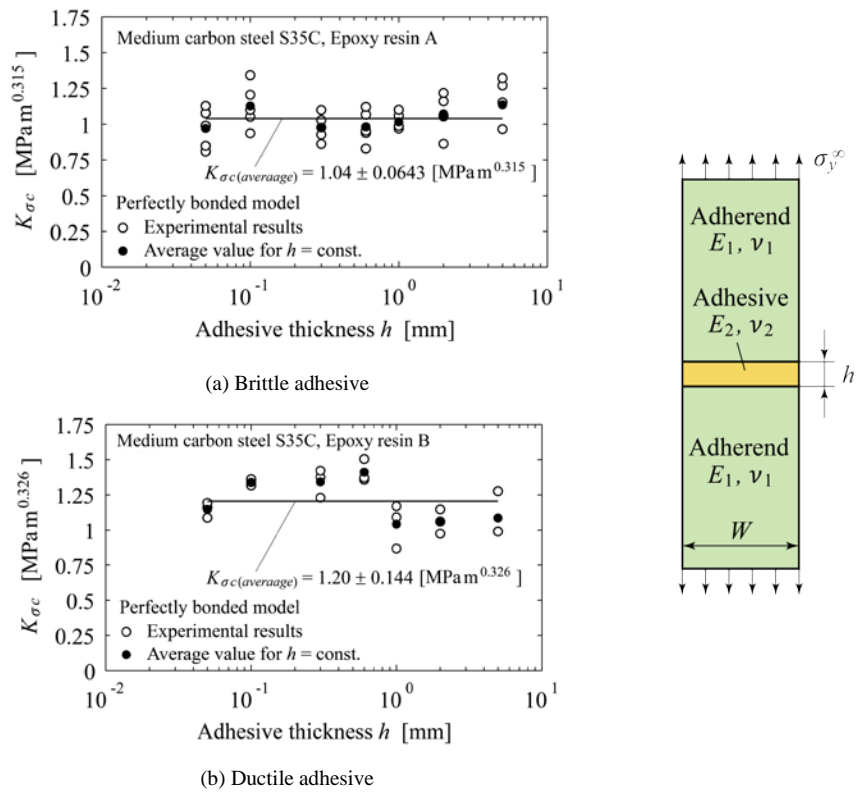


Fig.1 Adhesive strength expressed as $K_{\sigma_c} = \text{const.}$ for butt joint.

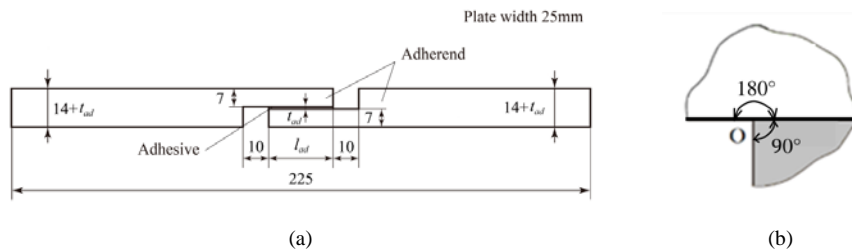


Fig. 2. Specimen configurations.

2. Outline of the analysis method proposed for butt joints

The most popular ISSF is known as the stress intensity factor for cracks. To obtain more general ISSF for evaluating interface strength, several analytical techniques were applied [Shibutani (2004); Hattori *et al.* (1988); Shiratori (1994); Kitamura *et al.* (2002); Shibutani *et al.* (2003); Takahashi *et al.* (2016); Hirata *et al.* (2006); Noda and Takase (2003)]. One of the most used numerical modelling technique is Finite Element Method, which can be used for many engineering applications conveniently [Noda *et al.* (2015a; 2015c; 2016; 2017); Wang *et al.* (2016); Miyazaki *et al.* (2017)]. Here, the brief outline of the mesh-independent technique coupled with FEM will be explained since the details were indicated for the butt joint [Noda *et al.* (2015b); Zhang *et al.* (2010); Zhang *et al.* (2015)]. By assuming homogeneous adhesive layer, it is known that the interface stress σ_y has singularity in the form $\sigma_y \propto 1/r^{1-\lambda}$ when $\alpha(\alpha-2\beta) > 0$ as shown in Fig.3. Here, α, β denote Dundurs' parameters [Dundurs (1969)] defined in Eq. (1) and the singular index λ can be determined from Eq. (2) [Bogy, (1968; 1971)] with the special angles for both adhesive 90° and adherend 90° as shown in Fig.1.

$$\alpha = \frac{G_1(\kappa_2 + 1) - G_2(\kappa_1 + 1)}{G_1(\kappa_2 + 1) + G_2(\kappa_1 + 1)}, \beta = \frac{G_1(\kappa_2 - 1) - G_2(\kappa_1 - 1)}{G_1(\kappa_2 + 1) + G_2(\kappa_1 + 1)}, \kappa_j = \begin{cases} \frac{3 - \nu_j}{1 + \nu_j} & \text{(plane stress)} \\ 3 - 4\nu_j & \text{(plane strain)} \end{cases} (j=1,2) \quad (1)$$

$$\left[\sin^2\left(\frac{\pi}{2}\lambda\right) - \lambda^2 \right]^2 \beta^2 + 2\lambda^2 \left[\sin^2\left(\frac{\pi}{2}\lambda\right) - \lambda^2 \right] \alpha\beta + \lambda^2(\lambda^2 - 1)\alpha^2 + \frac{\sin^2(\pi\lambda)}{4} = 0 \quad (2)$$

When $\alpha(\alpha-2\beta) > 0$, the eigenequation (2) has only one real root in the range $0 \leq \text{Re}(\lambda) \leq 1$. Then, the singular interface stress σ_y can be expressed as follows.

$$\sigma_y = \frac{K_\sigma}{r^{1-\lambda}} \quad (3)$$

Table 1 shows the FEM stress σ_y^{FEM} and the FEM stress ratio $\sigma_y^{\text{FEM}} / \sigma_y^{\text{FEM}*}$, where σ_y^{FEM} is the FEM stress of the bounded strip with $h/W=0.001$ in Fig.3(c), is the FEM stress of the bounded strip with $h/W \geq 1$ in Fig.3(d). It should be noted that the FEM stress σ_y^{FEM} is different from the real stress σ_y^{real} due to the finiteness of the mesh division. Here, it should be noted that the results of bonded plate for $h/W \geq 1$ are available as the exact reference solution obtained by the body force method as shown in Appendix A [Noda *et al.* (2007)]. The ratio $\sigma_y^{\text{FEM}} / \sigma_y^{\text{FEM}*}$ is independent of the mesh size, and therefore, as shown in Eq. (4), the ratio of ISSF K_σ / K_σ^* is determined from the FEM stress ratio $\lim_{r \rightarrow 0} [\sigma_y^{\text{FEM}}(r) / \sigma_y^{\text{FEM}*}(r)]$ although the real stress σ_y^{real} is not available. Here, an asterisk (*) means the values of the reference problem. The same FEM mesh pattern is applied to unknown problems and reference problems.

$$\frac{K_\sigma}{K_\sigma^*} = \frac{\lim_{r \rightarrow 0} [r^{1-\lambda} \times \sigma_y^{real}(r)]}{\lim_{r \rightarrow 0} [r^{1-\lambda} \times \sigma_y^{real*}(r)]} = \lim_{r \rightarrow 0} \frac{[\sigma_y^{FEM}(r)]}{[\sigma_y^{FEM*}(r)]} = \frac{\sigma_y^{FEM}(0)}{\sigma_y^{FEM*}(0)}, \quad (4)$$

$$K_\sigma = \lim_{r \rightarrow 0} [r^{1-\lambda} \times \sigma_y^{real}(r)] \neq \lim_{r \rightarrow 0} [r^{1-\lambda} \times \sigma_y^{FEM}(r)]$$

To obtain the ISSF from the FEM stress ratio, a reference solution in Fig.3 (b) is used because the exact ISSF has been investigated as shown in Appendix A. This method shown above is very convenient to analyze the ISSF by focusing on the FEM stress $\sigma_y^{FEM}(r \rightarrow 0)$.

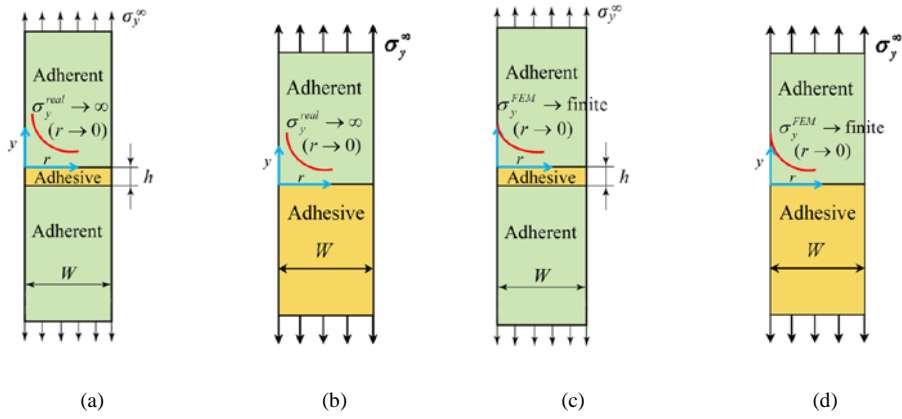


Fig. 3. Real stress σ_y^{real} for (a) butt joint, (b) bonded strip ($h/W \geq 1$) vs. FEM stress σ_y^{FEM} for (c) butt joint, (d) bonded strip ($h/W \geq 1$)

Table 1. FEM stress distributions $\frac{\sigma_y^{FEM}}{\sigma_y} \Big|_{h/W=0.001}$ stress distribution ratio $\frac{\sigma_y^{FEM}}{\sigma_y} \Big|_{h/W=0.001} / \frac{\sigma_y^{FEM}}{\sigma_y} \Big|_{h/W \geq 1}$ for bonded strip under tension shown in Fig. 3 obtained by different mesh size.

	Smallest mesh size $e_{\min} = 1/3^8$ around the edge		Smallest mesh size $e_{\min} = 1/3^4$ around the edge	
r/W	$\frac{\sigma_y^{FEM}}{\sigma_y} \Big _{h/W=0.001}$	$\frac{\sigma_y^{FEM} / \Big _{h/W=0.001}}{\sigma_y^{FEM} / \Big _{h/W \geq 1}}$	$\frac{\sigma_y^{FEM}}{\sigma_y} \Big _{h/W=0.001}$	$\frac{\sigma_y^{FEM} / \Big _{h/W=0.001}}{\sigma_y^{FEM} / \Big _{h/W \geq 1}}$
0	1.414	0.525	0	1.072
1/656100	1.177	0.525	1/81000	0.889
				0.524
				0.522

2/656100	1.138	0.525	2/81000	0.859	0.522
3/656100	1.109	0.525	3/81000	0.838	0.522
4/656100	1.088	0.525	4/81000	0.824	0.523
5/656100	1.071	0.525	5/81000	0.813	0.525

The ISSF for butt joints can be obtained conveniently because there is only one real root in Eq. (2) and the exact reference solution K_{σ}^* is available for bonded plate [Noda *et al.*(2007)]. Then, the adhesive strength can be expressed as a constant value of critical ISSF ($K_{\sigma c} = \text{const.}$) for both brittle and ductile adhesive butt joints as shown in Fig. 1 [Noda *et al.* (2015b)]. Although the Suzuki's specimen were carefully prepared for carbon steel/epoxy resin [Suzuki (1987)] to exclude the defect and residual strain, other experimental results also can be expressed as a constant value of critical ISSF ($K_{\sigma c} = \text{const.}$) for carbon steel/epoxy resin, aluminum/araldite, and brass/solder [Noda *et al.*(2015b)]. Those results suggested that the present method may be useful for evaluating other toughened structural adhesives exhibiting a good degree of ductility [Noda *et al.* (2015c); Wang *et al.* (2016); Miyazaki *et al.* (2017)]. In other words, if interface failure is confirmed instead of cohesive failure (see Fig.13), the linear elastic approach presented in this paper may predict the failure of a relatively ductile adhesive.

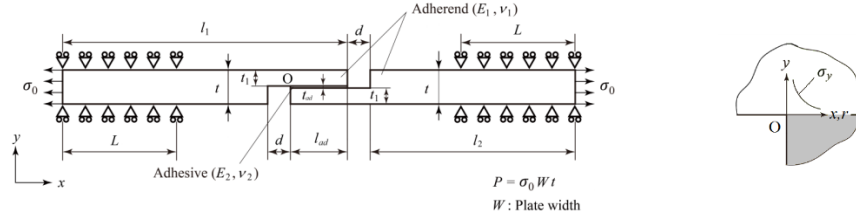


Fig. 4. Analysis model and boundary condition.

3. Analysis method for lap joints focusing on the distinct singular stress field

Lap joints have distinct singular stress fields at the interface end [Bogy (1971); Yuuki (1993)]. In this Section, the single lap joint in Fig.4 will be considered as an example of lap joints. The value of the singular index λ can be determined from the eigenequation (5), which was derived by Bogy (1968; 1971) with the special angles for adhesive 90° and adherend 180° as shown in Fig.2.

$$4 \sin^2(\pi\lambda) \left\{ \sin^2\left(\frac{\pi\lambda}{2}\right) - \lambda^2 \right\} \beta^2 + 4\lambda^2 \sin^2(\pi\lambda) \alpha\beta + \left\{ \sin^2\left(\frac{\pi\lambda}{2}\right) - \lambda^2 \right\} \alpha^2 - 4\lambda^2 \sin^2(\pi\lambda) \beta \quad (5)$$

$$- 2 \left\{ \lambda^2 \cos(2\pi\lambda) + \sin^2\left(\frac{\pi\lambda}{2}\right) \cos(\pi\lambda) + \frac{1}{2} \sin^2(\pi\lambda) \right\} \alpha + \sin^2\left(\frac{3\pi}{2}\lambda\right) - \lambda^2 = 0$$

Here, α, β are Dundurs' parameters [Dundurs (1969)] expressed from Poisson's ratio ν and shear modulus G ($j=1$ is for adhesive, $j=2$ is for adherend).

$$\alpha = \frac{G_1(\kappa_2 + 1) - G_2(\kappa_1 + 1)}{G_1(\kappa_2 + 1) + G_2(\kappa_1 + 1)}, \beta = \frac{G_1(\kappa_2 - 1) - G_2(\kappa_1 - 1)}{G_1(\kappa_2 + 1) + G_2(\kappa_1 + 1)}, \kappa_j = \begin{cases} \frac{3 - \nu_j}{1 + \nu_j} & \text{(plane stress)} \\ 3 - 4\nu_j & \text{(plane strain)} \end{cases} \quad (j = 1, 2) \quad (6)$$

Note that the eigenequation for lap joint has two real roots for most of material combination as shown in Appendix B.

The single lap joint testing for adhesive strength is standardized by Japanese Industrial Standards (JIS K6850) [JIS K6850 (1999)]. This standard prescribes the specimens with a small thickness 1.6 ± 0.1 mm. Since large bending deformations usually appear before debonding for thin specimens (see Fig.C.1), the thick specimens used by Park [Park *et al.* (2010)] in Fig.2 will be analyzed in this study, where the adherends aluminum alloy 6061-T6 are bonded with adhesive FM73M epoxy. The details of the specimens are indicated in Appendix C. Table 2 shows the elastic parameters of the adherend and adhesive. The eigenequation has two different real values, that is, $\lambda_1 = 0.6062$ and $\lambda_2 = 0.9989$. Then, the stresses σ_y and τ_{xy} can be expressed as follows.

$$\sigma_y = \frac{K_{\sigma, \lambda_1}}{r^{1-\lambda_1}} + \frac{K_{\sigma, \lambda_2}}{r^{1-\lambda_2}}, \tau_{xy} = \frac{K_{\tau, \lambda_1}}{r^{1-\lambda_1}} + \frac{K_{\tau, \lambda_2}}{r^{1-\lambda_2}}. \quad (7)$$

Table 2. Material properties of adhesive and adherent.

Material	Young's modulus E [GPa]	Poisson's ratio ν	α	β	λ_1	λ_2
Adherent 6061-T6	68.9	0.30	-0.8699	-0.06642	0.6062	0.9989
Adhesive Epoxy resin	4.20	0.45				

As shown in Eq. (7), the singular stress field of lap joint is complex and therefore the analysis is more difficult than the analysis of the butt joint. Since the method in Section 2 cannot be applied to the lap joint analysis directly, the singular stress field for the lap joint will be investigated.

Fig.4 shows the analysis model where l_1 and t_1 are the adherend length and adherend thickness, l_{ad} and t_{ad} are the adhesive length and adhesive thickness, L is the fixed boundary length of adherend, and σ_0 is the tension at both ends of single lap joint. In addition, (E_1, ν_1) and (E_2, ν_2) are Young's modulus and Poisson's ratio of the adherend and adhesive, respectively. The total length of the specimen in Fig. 4 is fixed as 225mm with varying the adhesive thickness $t_{ad} = 0.15 \sim 0.9$ mm and the adhesive length $l_{ad} = 10 \sim 50$ mm. Table 3 shows the dimensions of the specimens considered in this study.

Table 3. Dimensions of the adhesive joint specimens.

Specimen	l_{ad} [mm]	t_{ad} [mm]
A10	10	0.15
A15	15	0.15

A20	20	0.15
A25	25	0.15
A30	30	0.15
A35	35	0.15
A40	40	0.15
A50	50	0.15
A25-30	25	0.30
A25-45	25	0.45
A25-90	25	0.90
A30-30	30	0.30
A30-45	30	0.45
A30-90	30	0.90

Fig.5 shows the schematic illustration of the mesh pattern in the vicinity of the interface corner of the lap joint. The linear elastic analyses are performed under the plane strain condition by using the software MSC Marc. In this analysis, the elements near the edge corners of all models are set so as to be the same size and shape around the corner independent of the adhesive dimensions. Then, the minimum size of the element around the corner e_{\min} is changed, the effect of the mesh pattern on the stress distribution is investigated. The value of e_{\min} is set to 3^{-8} , 3^{-9} , 3^{-10} and 3^{-11} mm.

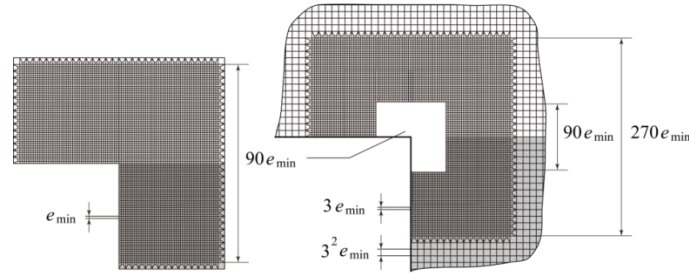


Fig. 5. Mesh pattern near the interface edge.

Table 4 shows the singular stress distributions obtained by FEM stress $\sigma_{y,FEM}$, $\tau_{xy,FEM}$ for the specimens A25, A50, A25-90 under the applied stress $\sigma_0 = 1$ MPa in Fig.4. Based on the fixed boundary length prescribed in JIS K6850 [JIS K6850 (1999)], $L = 50$ mm is fixed in this study. It is found that the stress ratios become almost constant independent of the minimum element size e_{\min} . Fig. 6 shows the normalized stress distribution $\sigma_{y,FEM}^{A50} / \sigma_{y,FEM}^{A25}$, $\tau_{xy,FEM}^{A50} / \tau_{xy,FEM}^{A25}$ under the applied stress $\sigma_0 = 1$ MPa in Fig.4. Fig. 7 shows the normalized stress distributions $\sigma_{y,FEM}^{A25-90} / \sigma_{y,FEM}^{A25}$, $\tau_{xy,FEM}^{A25-90} / \tau_{xy,FEM}^{A25}$ under the applied stress $\sigma_0 = 1$ MPa. From Fig.6, in the range of $10^{-3} > r > 10^{-4}$ mm, the stress ratios $\sigma_{y,FEM}^{A50} / \sigma_{y,FEM}^{A25}$ and $\tau_{xy,FEM}^{A50} / \tau_{xy,FEM}^{A25}$ are almost constant independent of r . However, from Fig.7, with decreasing r , $\sigma_{y,FEM}^{A25-90} / \sigma_{y,FEM}^{A25}$ and $\tau_{xy,FEM}^{A25-90} / \tau_{xy,FEM}^{A25}$ decreases rapidly. The stress distributions of the specimen A25-90 are different from those of the specimen A50 in this range. That is because the bending moment which is applied to the adhesive layer changes depending on the adhesive thickness. However, when the $r < 10^{-4}$ mm, $\sigma_{y0,FEM}^{A25-90} / \sigma_{y0,FEM}^{A25}$ and $\tau_{xy,FEM}^{A25-90} / \tau_{xy,FEM}^{A25}$ become almost constant.

Table 4. Stress distributions on the interface of specimens A25, A50 and A25-90 when $\sigma_0 = 1$ MPa.

(a) $e_{\min} = 3^{-8}$ mm

r [mm]	A25		A50		A25-90		$\frac{\sigma_{y,FEM}^{A50}}{\sigma_{y,FEM}^{A25}}$	$\frac{\tau_{xy,FEM}^{A50}}{\tau_{xy,FEM}^{A25}}$	$\frac{\sigma_{y,FEM}^{A25-90}}{\sigma_{y,FEM}^{A25}}$	$\frac{\tau_{xy,FEM}^{A25-90}}{\tau_{xy,FEM}^{A25}}$
	$\sigma_{y,FEM}^{A25}$	$\tau_{y,FEM}^{A25}$	$\sigma_{y,FEM}^{A50}$	$\tau_{y,FEM}^{A50}$	$\sigma_{y,FEM}^{A25-90}$	$\tau_{y,FEM}^{A25-90}$				
	[MPa]	[MPa]	[MPa]	[MPa]	[MPa]	[MPa]				
0/3 ⁸	108.089	-34.3491	82.2182	-26.1290	108.513	-34.4831	0.760653	0.760690	1.00392	1.00390
1/3 ⁸	60.9108	-17.5542	46.3257	-13.3538	61.1477	-17.6315	0.760550	0.760718	1.00389	1.00440
2/3 ⁸	45.8040	-14.9598	34.8342	-11.3807	45.9878	-15.0364	0.760506	0.760752	1.00401	1.00512
3/3 ⁸	36.3691	-13.4622	27.6575	-10.2414	36.5270	-13.5417	0.760467	0.760752	1.00434	1.00591
4/3 ⁸	31.0483	-12.2658	23.6104	-9.33110	31.1985	-12.3473	0.760441	0.760741	1.00484	1.00664
5/3 ⁸	27.6319	-11.3873	21.0119	-8.66264	27.7833	-11.4705	0.760422	0.760728	1.00548	1.00731
6/3 ⁸	25.2208	-10.6877	19.1718	-8.13018	25.3777	-10.7719	0.760158	0.760704	1.00622	1.00788

(b) $e_{\min} = 3^{-11}$ mm

r [mm]	A25		A50		A25-90		$\frac{\sigma_{y,FEM}^{A50}}{\sigma_{y,FEM}^{A25}}$	$\frac{\tau_{xy,FEM}^{A50}}{\tau_{xy,FEM}^{A25}}$	$\frac{\sigma_{y,FEM}^{A25-90}}{\sigma_{y,FEM}^{A25}}$	$\frac{\tau_{xy,FEM}^{A25-90}}{\tau_{xy,FEM}^{A25}}$
	$\sigma_{y,FEM}^{A25}$	$\tau_{y,FEM}^{A25}$	$\sigma_{y,FEM}^{A50}$	$\tau_{y,FEM}^{A50}$	$\sigma_{y,FEM}^{A25-90}$	$\tau_{y,FEM}^{A25-90}$				
	[MPa]	[MPa]	[MPa]	[MPa]	[MPa]	[MPa]				
0/3 ¹¹	396.766	-125.975	301.826	-95.8324	398.250	-126.441	0.760715	0.760726	1.00374	1.00370
1/3 ¹¹	224.377	-64.3886	170.680	-48.9821	225.258	-64.6264	0.760684	0.760726	1.00393	1.00369
2/3 ¹¹	169.059	-54.8550	128.597	-41.7302	169.735	-55.0544	0.760663	0.760736	1.00400	1.00364
3/3 ¹¹	134.534	-49.3942	102.333	-37.5760	135.084	-49.5722	0.760648	0.760737	1.00409	1.00360
4/3 ¹¹	115.084	-45.0352	87.5367	-34.2601	115.560	-45.1967	0.760633	0.760740	1.00414	1.00359
5/3 ¹¹	102.616	-41.8377	78.0522	-31.8277	103.046	-41.9899	0.760624	0.760742	1.00419	1.00364
6/3 ¹¹	93.8343	-39.2910	71.3715	-29.8904	94.2297	-39.4337	0.760612	0.760744	1.00421	1.00363

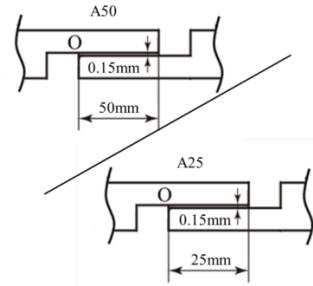
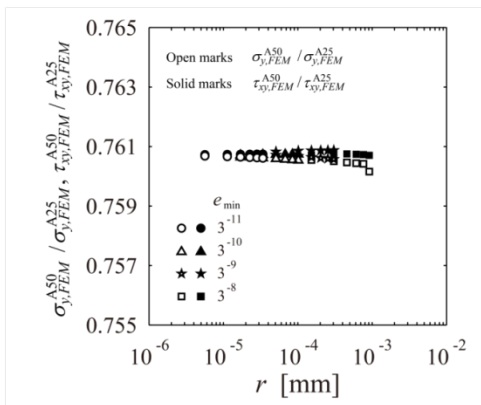
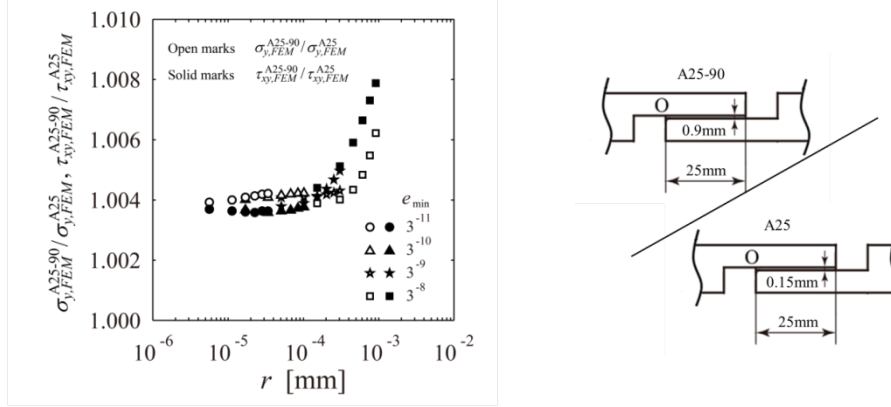


Fig. 6. Normalized stress distributions $\sigma_{y,FEM}^{A50} / \sigma_{y,FEM}^{A25}$, $\tau_{xy,FEM}^{A50} / \tau_{xy,FEM}^{A25}$ under $\sigma_0 = 1$ MPa.Fig. 7. Normalized stress distributions $\sigma_{y,FEM}^{A25-90} / \sigma_{y,FEM}^{A25}$, $\tau_{xy,FEM}^{A25-90} / \tau_{xy,FEM}^{A25}$ under $\sigma_0 = 1$ MPa.

From the results of Table 4 and Figs. 6, 7, it is found that the stress ratios at the edge corner become almost constant independent of e_{\min} , l_{ad} and l_{id} . Therefore, the following relations can be conjectured at the interface end.

$$\sigma_y = \frac{K_{\sigma,\lambda_1}}{r^{1-\lambda_1}} + \frac{K_{\sigma,\lambda_2}}{r^{1-\lambda_2}} \cong K_{\sigma,\lambda_1} \left(\frac{1}{r^{1-\lambda_1}} + \frac{C_\sigma}{r^{1-\lambda_2}} \right), \quad (8)$$

$$\tau_{xy} = \frac{K_{\tau,\lambda_1}}{r^{1-\lambda_1}} + \frac{K_{\tau,\lambda_2}}{r^{1-\lambda_2}} \cong K_{\tau,\lambda_1} \left(\frac{1}{r^{1-\lambda_1}} + \frac{C_\tau}{r^{1-\lambda_2}} \right) \quad (9)$$

Since the normalized stress is independent of the mesh size and the geometry of the adhesive joint, constant values C_σ and C_τ in Eqs. (8), (9) can be assumed. The validity of this assumption will be confirmed in the next Section.

The reference ISSF is denoted by K_{σ,λ_1}^* and the unknown ISSF is denoted by K_{σ,λ_1} . Then, the FEM stresses obtained at the corner point are denoted by $\sigma_{y0,FEM}^*$ for the reference solution and by $\sigma_{y0,FEM}$ for unknown problem. From Eq.(8), the relation between $K_{\sigma,\lambda_1} / K_{\sigma,\lambda_1}^*$ and $\sigma_{y0,FEM} / \sigma_{y0,FEM}^*$ can be expressed as follows.

$$\frac{K_{\sigma,\lambda_1}}{K_{\sigma,\lambda_1}^*} = \frac{\sigma_{y0,FEM}}{\sigma_{y0,FEM}^*} \quad (10)$$

If the reference ISSF K_{σ,λ_1}^* is available, the unknown ISSF K_{σ,λ_1} can be obtained from the FEM normal stress ratio $\sigma_{y0,FEM} / \sigma_{y0,FEM}^*$ by applying the same mesh pattern to the unknown and reference problems. Similarly, the unknown ISSF K_{τ,λ_1} can be obtained from the FEM shear stress ratio $\tau_{xy0,FEM} / \tau_{xy0,FEM}^*$ by using Eq. (11).

$$\frac{K_{\tau,\lambda_1}}{K_{\tau,\lambda_1}^*} = \frac{\tau_{xy0,FEM}}{\tau_{xy0,FEM}^*} \quad (11)$$

As shown in Fig. 6, it is found that the difference between $\sigma_{y0,FEM}^{A50}/\sigma_{y0,FEM}^{A25}$ and $\tau_{xy0,FEM}^{A50}/\tau_{xy0,FEM}^{A25}$ tends to become smaller with decreasing r . Then, from Fig. 7, the difference between $\sigma_{y0,FEM}^{A25-90}/\sigma_{y0,FEM}^{A25}$ and $\tau_{xy0,FEM}^{A25-90}/\tau_{xy0,FEM}^{A25}$ tends to become smaller with decreasing r . From Table 4, the relations of $\sigma_{y0,FEM}^{A50}/\sigma_{y0,FEM}^{A25} = \tau_{xy0,FEM}^{A50}/\tau_{xy0,FEM}^{A25}$ and $\sigma_{y0,FEM}^{A25-90}/\sigma_{y0,FEM}^{A25} = \tau_{xy0,FEM}^{A25-90}/\tau_{xy0,FEM}^{A25}$ can be confirmed. This means we have the equation $\sigma_{y0,FEM}/\sigma_{y0,FEM}^* = \tau_{xy0,FEM}/\tau_{xy0,FEM}^*$, and therefore, we have the equation (12).

$$\frac{K_{\sigma,\lambda_1}}{K_{\sigma,\lambda_1}^*} = \frac{K_{\tau,\lambda_1}}{K_{\tau,\lambda_1}^*} \quad (12)$$

From Eqs. (10)~(12), it is seen that similar equations can be obtained for K_{σ,λ_2} and K_{τ,λ_2} . This is because C_σ and C_τ are constant. Since the weaker singular index is close to no singularity as $\lambda_2 = 0.9989 \approx 1$, the stronger singular stress field with λ_1 is enough to be considered. Table 5 shows the singular indexes λ_1 , λ_2 of some other material combinations in [Zhang *et al.* (2015)] including stainless steel SUS304, aluminum alloy A7075, silicon and IC substrate FR-4.5 as the adherends with resin as the adhesive. It is found that the weaker singular indexes λ_2 is in the small range of 0.9914~0.9999.

Table 5. Singular indexes for single lap joint with different material combinations.

	Material	Young's modulus E [GPa]	Poisson's ratio ν	λ_1	λ_2
Adherent	SUS304(stainless steel)	206	0.3	0.6568	0.9999
	A7075(aluminum alloys)	71	0.33	0.6489	0.9995
	Silicon	166	0.26	0.6552	0.9999
	FR-4.5(IC substrate)	15.34	0.15	0.6020	0.9914
Adhesive	Resin	2.74	0.38		

4. Discussion for evaluating the singular stress field of lap joint

In Section 3, a convenient evaluation method was presented to obtain the ISSF of single lap joint. It was found that the singular stress field is expressed in a similar way almost independent of the geometry of the adhesive joint. However, only the normalized singular stress field can be discussed by using this method from Eqs. (10~12). The ISSF cannot be obtained since there is no exact reference solution for the lap joint. In this Section, therefore, the reference solution will be obtained by using the reciprocal work contour integral method (RWCIM) [Carpenter and Byers (1987)], and the usefulness of the proposed method in Section 3 will be verified by comparing the results of RWCIM. The detail of RWCIM is indicated in Appendix D.

Around interface corner O in Fig.4, the stresses σ_θ and $\tau_{r\theta}$ in the r direction can be expressed as follows. The notation r denotes the radial distance away from the corner singular point O.

$$\begin{aligned}\sigma_\theta &= \frac{K_1}{r^{1-\lambda_1}} f_{\theta\theta}(\theta, \lambda_1) + \frac{K_2}{r^{1-\lambda_2}} f_{\theta\theta}(\theta, \lambda_2), \\ \tau_{r\theta} &= \frac{K_1}{r^{1-\lambda_1}} f_{r\theta}(\theta, \lambda_1) + \frac{K_2}{r^{1-\lambda_2}} f_{r\theta}(\theta, \lambda_2).\end{aligned}\quad (13)$$

Here, K_k ($k=1,2$) has real values, the $f_{\theta\theta}(\theta, \lambda_k)$ and $f_{r\theta}(\theta, \lambda_k)$ are non-dimensional functions of angle θ and λ_k . Three boundaries exist in a bi-material open wedge such as the one shown in Fig.4, two traction free edges (at angles $\theta = -\pi/2$ and $\theta = \pi$) and an interface ($\theta=0$). By focusing on the interface stress, the intensity of singular stress fields ISSFs are controlled by the following four parameters.

$$\begin{aligned}K_1 f_{\theta\theta}(\theta, \lambda_1) \Big|_{\theta=0} &= K_{\sigma, \lambda_1}, \quad K_2 f_{\theta\theta}(\theta, \lambda_2) \Big|_{\theta=0} = K_{\sigma, \lambda_2}, \\ K_1 f_{r\theta}(\theta, \lambda_1) \Big|_{\theta=0} &= K_{\tau, \lambda_1}, \quad K_2 f_{r\theta}(\theta, \lambda_2) \Big|_{\theta=0} = K_{\tau, \lambda_2}.\end{aligned}\quad (14)$$

As shown in Eq.(14), since the four parameters K_{σ, λ_1} , K_{σ, λ_2} , K_{τ, λ_1} , K_{τ, λ_2} are determined from K_1 and K_2 , the singular stress field is also determined by the two real parameters.

Fig. 8 shows the integral path for RWCIM. The linear elastic analyses are performed under the plane strain condition by using the software MSC Marc. Fig. 9 shows the schematic illustration of the mesh pattern in the present analyses. Here, 8-node elements are used in the vicinity of the interface corner edge, 4-node elements are used in other regions.

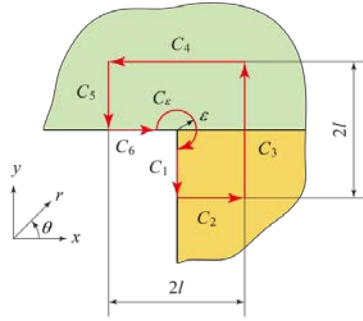


Fig. 8. Integral path c for RWCIM ($C = C_1 + C_2 + C_3 + C_4 + C_5 + C_6 + C_\epsilon$).

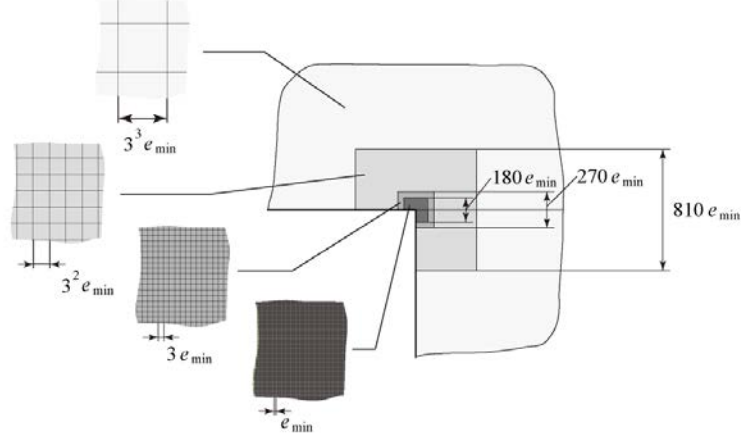


Fig. 9. Mesh pattern near the interface edge corner.

The analysis results of the specimen A25 under $\sigma_0 = 1$ MPa are shown as follows. The contour integral path C in Fig. 8 and the mesh pattern in Fig. 9 are used in order to calculate the ISSF. Table 6 shows K_{σ, λ_1} , K_{σ, λ_2} , K_{τ, λ_1} , K_{τ, λ_2} by varying e_{\min} and l/e_{\min} where l is the path dimension in Fig.8 and e_{\min} is the minimum mesh dimension in Fig.9. As shown in Table 6, the ISSFs with stronger singularity can be obtained as $K_{\sigma, \lambda_1} = -0.1010$ and $K_{\tau, \lambda_1} = -0.04723$ when $l/e_{\min} \geq 10$. Similarly, the ISSFs with weaker singularity can be obtained as $K_{\sigma, \lambda_2} = -0.5485$ and $K_{\tau, \lambda_2} = -0.01168$ when l/e_{\min} is large enough. Fig. 10 shows the interface stress σ_y and τ_{xy} as solid curves obtained by substituting those ISSFs into Eq.(7). Here, the circle mark denotes the FEM stress σ_y and the triangle marks denotes the FEM stress τ_{xy} . When $r \leq 0.01$ mm, the FEM stresses are in good agreement with the solid curves. The values of FEM stresses varies by varying e_{\min} , however, the marks are always in good agreement with the solid curves when e_{\min} is small enough.

 Table 6. ISSFs K_{σ, λ_1} , K_{σ, λ_2} , K_{τ, λ_1} , K_{τ, λ_2} obtained by varying the minimum mesh size e_{\min} .

l/e_{\min}	$e_{\min} = 3^{-11}$ mm				$e_{\min} = 3^{-9}$ mm			
	K_{σ, λ_1}	K_{σ, λ_2}	K_{τ, λ_1}	K_{τ, λ_2}	K_{σ, λ_1}	K_{σ, λ_2}	K_{τ, λ_1}	K_{τ, λ_2}
5	0.1010	-0.5347	-0.04727	-0.01139	0.1011	-0.5511	-0.04728	-0.01174
10	0.1010	-0.5440	-0.04724	-0.01158	0.1010	-0.5497	-0.04724	-0.01171
20	0.1010	-0.5500	-0.04724	-0.01171	0.1010	-0.5484	-0.04724	-0.01168
40	0.1010	-0.5472	-0.04723	-0.01165	0.1010	-0.5485	-0.04723	-0.01168
80	0.1010	-0.5485	-0.04723	-0.01168	0.1010	-0.5486	-0.04723	-0.01168

$$K_{\sigma, \lambda_1}, K_{\tau, \lambda_1} : \text{MPa} \cdot \text{m}^{1-\lambda_1}, \quad K_{\sigma, \lambda_2}, K_{\tau, \lambda_2} : \text{MPa} \cdot \text{m}^{1-\lambda_2}$$

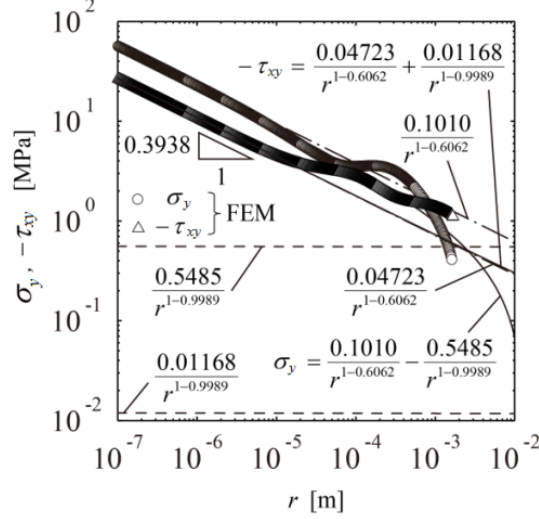


Fig. 10. Comparison between stress distribution of Specimen A 25 by Eq. (7) and FEM.

Since Section 3 shows the stress distribution normalized by the results of A25, the specimen geometry of A25 in Table 3 is analyzed by RWCIM and indicated in Table 6. Table 7 shows all the results in Table 3 obtained from Eqs. (10), (11) with Table 6 by RWCIM. The same FEM mesh pattern is applied to unknown problems and reference problems. Table 7 also shows the results obtained by applying RWCIM directly to all geometries in Table 3. The results with the stronger stress singularity λ_1 agree well with the RWCIM's results although small difference can be seen for the results for weaker stress singularity λ_2 . It may be concluded that the proposed method with the reference solution provides the ISSF conveniently. In addition, the normalized ISSF can be obtained more easily without the reference solution. Then they can predict the strength of adhesive joint accurately and conveniently.

Table 8 shows the ratios of $K_{\sigma, \lambda_2}/K_{\sigma, \lambda_1}$, $K_{\tau, \lambda_2}/K_{\tau, \lambda_1}$ and $K_{\tau, \lambda_1}/K_{\sigma, \lambda_1}$, $K_{\tau, \lambda_2}/K_{\sigma, \lambda_2}$. Because K_{σ, λ_1} and K_{τ, λ_1} are defined from K_1 as shown in Eq. (14), the $K_{\tau, \lambda_1}/K_{\sigma, \lambda_1}$ is always constant as $K_{\tau, \lambda_1}/K_{\sigma, \lambda_1} \equiv -0.4678$ independent of l_{ad} , t_{ad} . Similarly, $K_{\tau, \lambda_2}/K_{\sigma, \lambda_2}$ is also always constant as $K_{\tau, \lambda_2}/K_{\sigma, \lambda_2} \equiv 0.02130$. In the experiment, the cohesive fracture occurs when $l_{ad} < 15\text{mm}$ (specimens A10 and A15) and the adhesive fracture occurs when $l_{ad} > 15\text{mm}$ as indicated in Appendix C. Except for the models A10 and A15, the values of $K_{\sigma, \lambda_2}/K_{\sigma, \lambda_1}$ and $K_{\tau, \lambda_2}/K_{\tau, \lambda_1}$ are in the smaller ranges as $K_{\sigma, \lambda_2}/K_{\sigma, \lambda_1} = -5.574 \sim -4.827$ and $K_{\tau, \lambda_2}/K_{\tau, \lambda_1} = 0.2198 \sim 0.2538$, insensitive to l_{ad} and t_{ad} .

Table 7(a) Comparison of ISSFs K_{σ, λ_1} , K_{τ, λ_1} obtained by using Eq. (10) and RWCIM.

Specimen	K_{σ, λ_1} [MPa · m ^{1-λ_1}]	K_{τ, λ_1} [MPa · m ^{1-λ_1}]
----------	--	--

	K_{σ,λ_1} by using	K_{σ,λ_1} by using	Error(%)	K_{τ,λ_1} by using	K_{τ,λ_1} by using	Error(%)
	Eq.(10)	RWCIM		Eq.(11)	RWCIM	
A25(Ref)	0.1010	0.1010	0	-0.04723	-0.04723	0
A10	0.1065	0.1065	-0.0063	-0.0498	-0.04981	-0.0109
A15	0.1084	0.1083	0.0706	-0.05068	-0.05068	0.0024
A20	0.1056	0.1056	0.0241	-0.04938	-0.0494	-0.0127
A30	0.09609	0.09606	0.0303	-0.04493	-0.04723	-0.0130
A35	0.09111	0.09107	0.0396	-0.0426	-0.04494	-0.0137
A40	0.08621	0.08618	0.0359	-0.04032	-0.04261	-0.0121
A50	0.07682	0.07680	0.0295	-0.03593	-0.04032	-0.0131
A25-30	0.09801	0.09796	0.0471	-0.04583	-0.03593	-0.0043
A25-45	0.09782	0.09777	0.0500	-0.04574	-0.04583	-0.0011
A25-90	0.1013	0.1013	0.0288	-0.04738	-0.04574	-0.0006
A30-30	0.09298	0.09294	0.0444	-0.04348	-0.04738	-0.0031
A30-45	0.09250	0.09246	0.0456	-0.04325	-0.04348	0.0083
A30-90	0.09487	0.09482	0.0510	-0.04436	-0.04325	-0.0030

Table 7 (b). Comparison of ISSFs K_{σ,λ_2} and K_{τ,λ_2} obtained by using Eq. (10) and RWCIM.

Specimen	K_{σ,λ_2} [MPa · m ^{1-λ₂}]			K_{τ,λ_2} [MPa · m ^{1-λ₂}]		
	K_{σ,λ_2} by using	K_{σ,λ_2} by using	Error(%)	K_{τ,λ_2} by using	K_{τ,λ_2} by using	Error(%)
	Eq.(10)	RWCIM		Eq.(11)	RWCIM	
A25(Ref)	-0.5485	-0.5485	0	-0.01168	-0.01168	0
A10	-0.5783	-0.6469	-10.600	-0.01232	-0.01378	-10.619
A15	-0.5886	-0.6021	-2.2489	-0.01253	-0.01282	-2.2349
A20	-0.5736	-0.5735	0.0208	-0.01222	-0.01222	-0.0402
A30	-0.5218	-0.5237	-0.3570	-0.01111	-0.01168	-0.4279
A35	-0.4948	-0.4985	-0.7484	-0.01054	-0.01116	-0.7907
A40	-0.4682	-0.4741	-1.2476	-0.01000	-0.01062	-1.2876
A50	-0.4172	-0.4280	-2.5233	-0.00889	-0.00912	-2.5627
A25-30	-0.5322	-0.5022	5.9819	-0.01133	-0.01070	5.9186
A25-45	-0.5312	-0.4884	8.7683	-0.01131	-0.01040	8.7635
A25-90	-0.5503	-0.4888	12.579	-0.01172	-0.01041	12.555
A30-30	-0.5050	-0.4785	5.5283	-0.01075	-0.01019	5.5181
A30-45	-0.5024	-0.4644	8.1720	-0.01070	-0.00989	8.1233
A30-90	-0.5152	-0.4631	11.251	-0.01097	-0.00987	11.200

Table 8. ISSF ratios $K_{\sigma,\lambda_2}/K_{\sigma,\lambda_1}$, $K_{\tau,\lambda_2}/K_{\tau,\lambda_1}$, $K_{\tau,\lambda_1}/K_{\sigma,\lambda_1}$, $K_{\tau,\lambda_2}/K_{\sigma,\lambda_2}$.

Specimen	$K_{\sigma,\lambda_2}/K_{\sigma,\lambda_1} = C_\sigma$	$K_{\tau,\lambda_2}/K_{\tau,\lambda_1} = C_\tau$	$K_{\tau,\lambda_1}/K_{\sigma,\lambda_1}$	$K_{\tau,\lambda_2}/K_{\sigma,\lambda_2}$
A10	-6.075	0.2766	-0.4678	0.02130
A15	-5.557	0.2530	-0.4678	0.02130
A20	-5.431	0.2473	-0.4678	0.02130
A25	-5.430	0.2473	-0.4678	0.02130
A30	-5.452	0.2483	-0.4678	0.02130
A35	-5.474	0.2492	-0.4678	0.02130
A40	-5.501	0.2505	-0.4678	0.02130
A50	-5.574	0.2538	-0.4678	0.02130
A25-30	-5.125	0.2334	-0.4678	0.02130
A25-45	-4.995	0.2274	-0.4678	0.02130
A25-90	-4.827	0.2198	-0.4678	0.02130
A30-30	-5.148	0.2344	-0.4678	0.02130
A30-45	-5.022	0.2287	-0.4678	0.02130
A30-90	-4.885	0.2224	-0.4678	0.02130

Therefore, interface stresses σ_y and τ_{xy} may be expressed by the following equation.

$$\sigma_y \cong \frac{K_{\sigma,\lambda_1}}{r^{1-\lambda_1}}(1 + C_\sigma r^{\lambda_2-\lambda_1}), \quad \tau_{xy} \cong \frac{K_{\tau,\lambda_1}}{r^{1-\lambda_1}}(1 + C_\tau r^{\lambda_2-\lambda_1}) \quad (15)$$

Here, C_σ and C_τ are almost constant expressed as $C_\sigma = -5.3213 \pm 0.3379$, $C_\tau = 0.2423 \pm 0.0154$ as shown in Table 8. Fig.11 shows $\sigma_y/(K_{\sigma,\lambda_1}/r^{1-\lambda_1})$ and $\tau_{xy}/(K_{\tau,\lambda_1}/r^{1-\lambda_1})$ for all specimens except for A10 and A15. The dashed line shows the results of A50 and the dashed-dotted line shows the results of A25-90. It is found that all curves are within the thin gray area between A50 and A25-90. In other words, the singular stress fields of all the specimens are similar. Since $\sigma_y/(K_{\sigma,\lambda_1}/r^{1-\lambda_1}) = 0.94 \sim 1$ and $\tau_{xy}/(K_{\tau,\lambda_1}/r^{1-\lambda_1}) \cong 1$, the effects of $K_{\sigma,\lambda_2}/r^{1-\lambda_2}$ and $K_{\tau,\lambda_2}/r^{1-\lambda_2}$ in Eqs.(8), (9) are very small. Since K_{σ,λ_1} and K_{τ,λ_1} are defined from K_1 as shown in Eq. (14), the ISSF can be represented by K_{σ,λ_1} as discussed in Section 3.

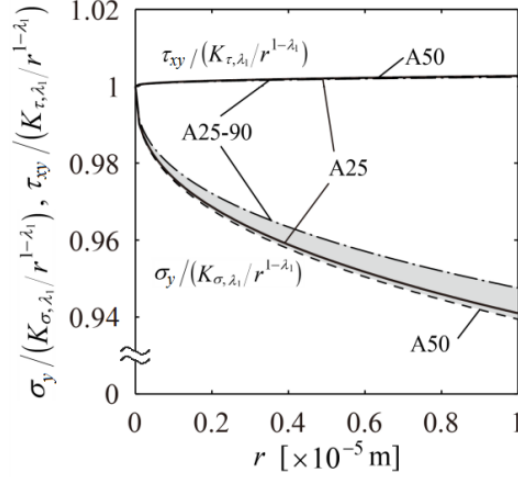


Fig. 11. Normalized stress distributions $\sigma_y / (K_{\sigma, \lambda_1} / r^{1-\lambda_1})$, $\tau_{xy} / (K_{\tau, \lambda_1} / r^{1-\lambda_1})$.

Therefore, the ISSF of lap joints as well as butt joints can be obtained conveniently by using the analysis method presented in this paper. It is found that although the singular stress is controlled by two factors for lap joints, it can be expressed almost similarly even if the adhesive geometries are changed widely. Since RWCIM requires the complex and difficult calculations such as matrix operation and numerical integration, the proposed method in Section 3 is found to be very convenient and practical to determine ISSF.

5. Adhesive strength expressed as a constant value of critical ISSF ($K_{\sigma_c} = \text{const.}$)

In this Section, the adhesive strength of single lap joint will be investigated by using the experimental results in Appendix C. Fig. 12 shows K_{σ, λ_1} under $\sigma_0 = 1$ MPa by varying the adhesive length l_{ad} . It is seen that K_{σ, λ_1} decreases when $l_{ad} \geq 15$ mm. Fig. 13(a) shows the critical average shear stress τ_c . When l_{ad} is smaller than about 15 mm, τ_c becomes constant at about 27.8 MPa. However, when l_{ad} is larger than about 15 mm, τ_c tends to decrease. The experimental observation shows that when $l_{ad} < 15$ mm the cohesive fracture occurs and K_{σ_c} increases. Fig. 13 (b) shows the critical ISSF $K_{\sigma_c} = \text{const.}$ when the debonding occurs under $\sigma_o = \sigma_c$ by varying l_{ad} . When $l_{ad} > 15$ mm, the adhesive fracture occurs and K_{σ_c} becomes constant independent of l_{ad} . The solid line shows the average value of K_{σ_c} for all specimens except for specimens A10 and A15. The open circle marks are distributed near the solid line within about 10% error. Nono and Nagahiro [1986] and Rodríguez *et al.* [2012] discussed the adhesive joint strength with varying adhesive geometries. If the adhesive length l_{ad} is short enough, the yielding may occur at the entire adhesive region before the ISSF at the interface end reaches the critical value, and therefore, cohesive failure occurs instead of

interface failure [Nono *et al.* (1986); Rodríguez *et al.* (2012)]. The previous studies suggested that the linear elastic approach with a critical ISSF=const. may be useful for evaluating other toughened structural adhesives exhibiting a good degree of ductility [Noda *et al.* (2015c); Wang *et al.* (2016); Miyazaki *et al.* (2017)]. In other words, if interface failure is confirmed instead of cohesive failure (see Fig.13), the presented method may predict the failure of a relatively ductile adhesive.

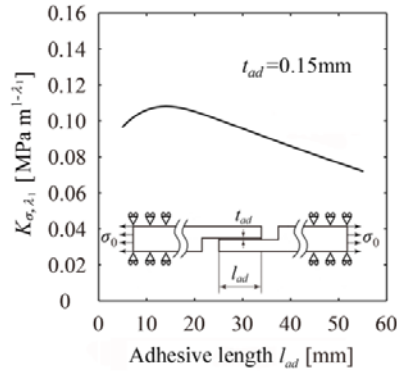


Fig. 12. Relationship between K_{σ, λ_1} and l_{ad} under $\sigma_0 = 1$ MPa.

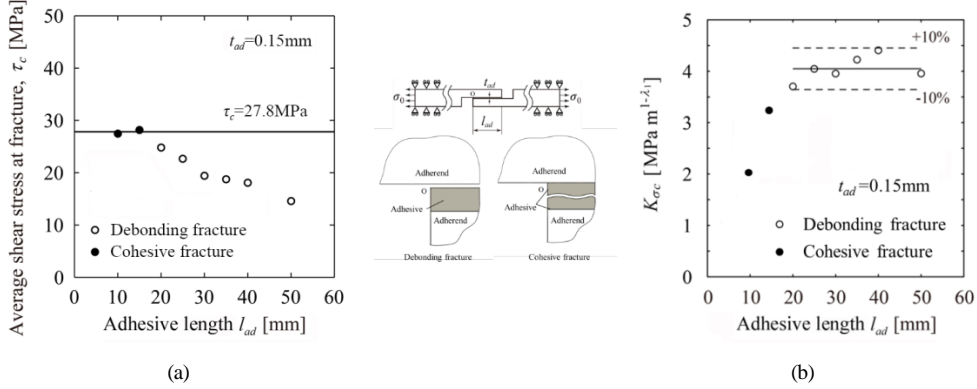


Fig. 13. (a) Average shear stress at fracture of specimens with $t_{ad} = 0.15$ mm, (b) Relationship between $K_{\sigma_c} = K_{\sigma, \lambda_1} |_{\sigma_0 = \sigma_c}$ and l_{ad} .

Fig. 14 shows the relationship between K_{σ, λ_1} and adhesive thickness t_{ad} under $\sigma_0 = 1$ MPa. The solid line and dashed line denote the values of K_{σ, λ_1} for $l_{ad} = 25$ mm and 30 mm, respectively. It is found that the K_{σ, λ_1} is almost constant independent of t_{ad} . Fig. 15 shows the relationship between K_{σ_c} and t_{ad} under $\sigma_0 = \sigma_c$. The results of K_{σ_c} are plotted in Fig.15 (a) for the specimens without guide block and in Fig.15 (b) for the specimens with guide block. It is seen that the strength is improved by using the guide block. This is because the size and number of the internal voids decrease by using the

guide block. The details are indicated in Appendix C. It is found that the values of K_{σ_c} are almost constant independent of t_{ad} even if changing the testing method.

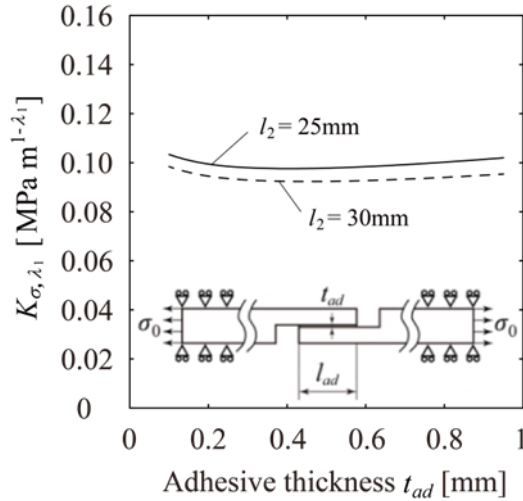


Fig.14. Relationship between K_{σ_c, λ_1} and t_{ad} when $\sigma_0 = 1$ MPa.

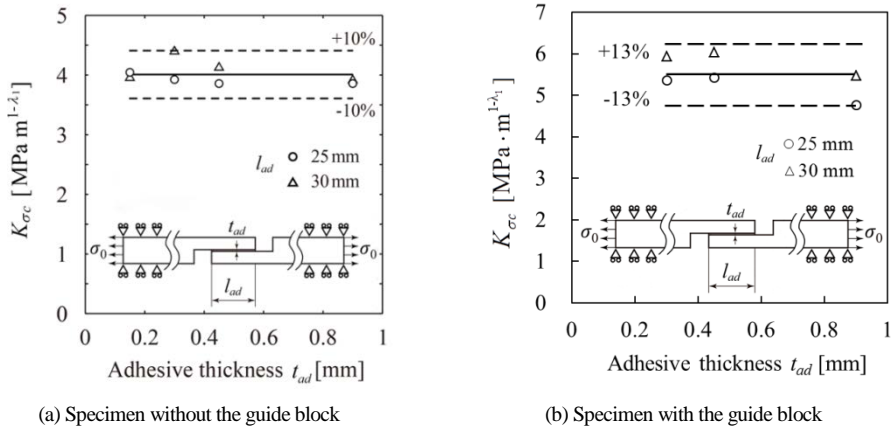


Fig. 15. Relationship between $K_{\sigma_c} = K_{\sigma_c, \lambda_1} |_{\sigma_0 = \sigma_c}$ and t_{ad} .

Fig. 16 shows the critical K_{σ_c} of all specimens except for specimens A10 and A15. The solid line shows the average values $K_{\sigma_c, ave} = 4.030 \text{ MPa} \cdot \text{m}^{1-\lambda_1}$ for the specimens without guide block, and $K_{\sigma_c, ave} = 5.499 \text{ MPa} \cdot \text{m}^{1-\lambda_1}$ for the specimens with guide block. The critical ISSFs K_{σ_c} are distributed within 10% error as shown in Fig. 16(a) and within 13% as shown in Fig. 16(b). It can be confirmed that the K_{σ_c} is almost constant independent of the l_{ad} and t_{ad} . Therefore, the debonding criterion of single

lap joints can be described as a constant value of critical ISSF $K_{\sigma_c} = \text{const.}$

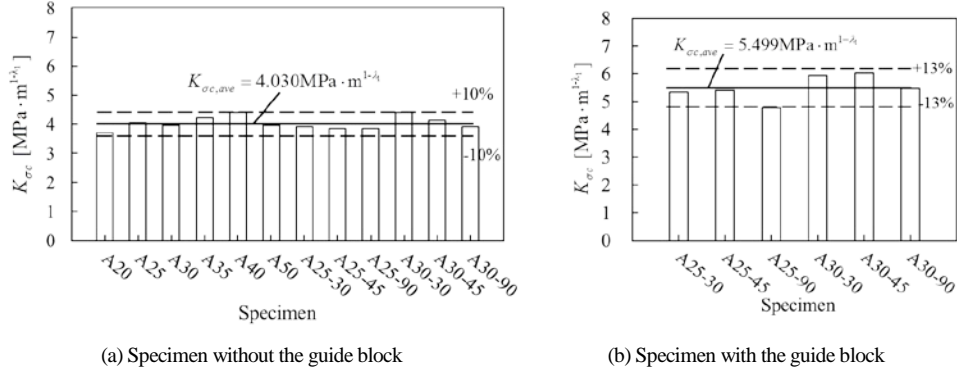


Fig. 16. Comparison between K_{σ_c} values.

In this Section, the value of K_{σ_c} is investigated based on the experimental result. It is found that the adhesive strength can be expressed as a constant value of critical ISSF $K_{\sigma_c} = \text{const.}$ Since the experiments are often time-consuming, the proposed FEM calculation is helpful for predicting the adhesive strength accurately and conveniently.

6. Conclusions

- (1) In this study, a convenient evaluation method of adhesive strength is presented in terms of the ISSF (intensity of singular stress field). In this method, the same mesh pattern is applied to the unknown problems and the reference problems by focusing on the FEM stress at the interface corner.
- (2) Although the singular stress is controlled by two factors for lap joints, it is found that the debonding condition can be expressed almost in the same way even if the adhesive geometries are widely changed. Therefore, the ISSF of lap joints as well as butt joints can be obtained conveniently by using the analysis method presented in this paper.
- (3) Based on the obtained ISSF, the debonding criterion is examined with varying the adhesive geometries. The results show that the adhesive strength can be expressed as $K_{\sigma_c} = \text{const}$ when the debonding fracture occurs.
- (4) The usefulness of the present solution is verified by comparing with the results of the conventional method (RWCIM). Since RWCIM requires the complex and difficult calculations such as matrix operation and numerical integration, the proposed method is found to be very convenient and practical to determine ISSF.

Acknowledgments

The research for this paper was financially supported by the Ministry of Education research expenses [grant number: 15K14150].

Appendix A. Reference solution useful for butt joint analysis: ISSF (intensity of singular stress field) for bonded strip under arbitrary material combinations

The ISSF (intensity of singular stress field) for butt joints in Fig. 3(c) can be obtained conveniently by using the exact reference solution F_{σ}^* shown in this appendix from the ratio as shown in Eq. (4) [Zhang *et al.* (2015)]. Fig. A.1 and Table A.1 indicate F_{σ}^* values for bonded strip, which are equivalent to the butt joint for $l/W \geq 1$.

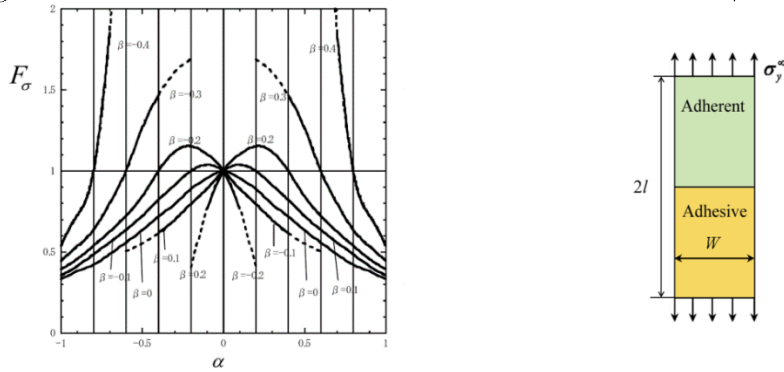


Fig. A.1. F_{σ}^* at interface edge point in bonded finite plate

Table A.1 F_{σ}^* at interface edge point in bonded plate. [underlined figures indicate $\lambda < 1$, **bold** figures indicate $\lambda > 1$, standard style figures indicate $\lambda = 1$]

α	$\beta = -0.4$	$\beta = -0.3$	$\beta = -0.2$	$\beta = -0.1$	$\beta = 0$	$\beta = 0.1$	$\beta = 0.2$	$\beta = 0.3$	$\beta = 0.4$
-1.0	0.540	0.446	0.395	0.357	0.332				
-0.95	0.643	0.491	0.422	0.381	0.349				
-0.9	0.726	0.534	0.456	0.412	0.381				
-0.8	1.000	0.636	0.538	0.487	0.45				
-0.7	1.855	0.800	0.626	0.558	0.486				
-0.6	3.291	1.000	0.724	0.638	0.559	0.505			
-0.5		1.264	0.842	0.722	0.635	0.551			
-0.4		1.467	1.000	0.822	0.718	0.615			
-0.3		1.609	1.118	0.913	0.796	0.697			
-0.2		1.690	1.153	1.000	0.889	0.797	0.404		
-0.1			1.103	1.037	0.955	0.890	0.767		
0			1.000	1.000	1.000	1.000	1.000		
0.1			0.767	0.890	0.955	1.037	1.103		
0.2			0.404	0.797	0.889	1.000	1.153	1.690	
0.3				0.697	0.796	0.913	1.118	1.609	
0.4				0.615	0.718	0.822	1.000	1.467	
0.5				0.551	0.635	0.722	0.842	1.264	
0.6				0.505	0.559	0.638	0.724	1.000	3.291
0.7					0.486	0.558	0.626	0.800	1.855
0.8					0.450	0.487	0.538	0.636	1.000
0.9					0.381	0.412	0.456	0.534	0.726
0.95					0.349	0.381	0.422	0.491	0.643
1.0					0.332	0.357	0.395	0.446	0.540

Since the single lap joint does not have any exact reference solutions, a calculation method to obtain reference solutions is indicated in Appendix D for the lap joint.

Appendix B. Singular index for lap joints

Table B. 1 shows singular index for lap joints λ within a range of $0 < \text{Re}(\lambda) < 1$, where the underlined figure indicate the multiple root, the bold figure indicate the complex root, the standard style figure indicate the real root. The eigenequation (5) has real root, multiple real root or complex root depending on (α, β) except for no root at $(\alpha, \beta) = (-1, -0.5)$. Two real roots appear in most of the material combinations.

Table B.1. Singular index for lap joints λ ($0 < \text{Re}(\lambda) < 1$). [underlined figure indicate multiple root, **bold** figure indicate complex root, standard style figure indicate real root]

α	$\beta = -0.5$	$\beta = -0.4$	$\beta = -0.3$	$\beta = -0.2$	$\beta = -0.1$	$\beta = 0$	$\beta = 0.1$	$\beta = 0.2$	$\beta = 0.3$	$\beta = 0.4$	$\beta = 0.5$
-1	Non	0.80731	0.72053	0.66461	0.62466	0.59461					
-0.9		0.80010	0.71327	0.65797	0.61866	0.58922					
-0.8		0.99732	0.99867	0.99911	0.99933	0.99947					
-0.7		0.79489	0.70660	0.65160	0.61282	0.58393					
-0.6		0.98860	0.99436	0.99625	0.99719	0.99775					
-0.5		0.792038	0.70053	0.64549	0.60712	0.57874					
-0.4		0.972568	0.98658	0.99107	0.99330	0.99464					
-0.3		0.792544	0.69510	0.63964	0.60155	0.57362	0.55253				
-0.2		0.947656	0.97479	0.98319	0.98738	0.98989	0.99156				
-0.1			0.69036	0.63404	0.59610	0.56860	0.54800				
0			0.95849	0.97222	0.97907	0.98320	0.98597				
0.1			0.68648	0.62872	0.59078	0.56365	0.54355				
0.2			0.93730	0.95776	0.96802	0.97425	0.97844				
0.3			0.68371	0.62369	0.58558	0.55876	0.53917				
0.4			0.91100	0.93952	0.95387	0.96266	0.96862				
0.5			0.68254	0.61899	0.58050	0.55394	0.53485	0.52105			
0.6			0.87940	0.91734	0.93630	0.94806	0.95611	0.96200			
0.7				0.61470	0.57554	0.54918	0.53061	0.51748			
0.8				0.89119	0.91512	0.93010	0.94051	0.94818			
0.9				0.61093	0.57071	0.54448	0.52643	0.51404			
1.0				0.86118	0.89024	0.90853	0.92139	0.93099			
1.1				0.60789	0.56602	0.53984	0.52234	0.51077			
1.2				0.82743	0.86174	0.88319	0.89841	0.90991			
1.3				0.60600	0.56151	0.53524	0.51834	0.50770	0.50185		
1.4				0.78989	0.82980	0.85410	0.87134	0.88446	0.89489		
1.5					0.55722	0.53070	0.51446	0.50492	0.50053		
1.6					0.79463	0.82136	0.84007	0.85426	0.86552		
1.7					0.55325	0.52620	0.51071	0.50254	0.50000		
1.8					0.75640	0.78519	0.80464	0.81903	0.83017		

0.5	0.54980	0.52174	0.50717	0.50076	0.50074					
	0.71511	0.74579	0.76513	0.77857	0.78813					
0.6	0.54739	0.51732	0.50394	0.50000	0.50374	0.51528				
	0.67032	0.70333	0.72160	0.73258	0.73835	0.73937				
0.7		0.51294	0.50130	0.50127	0.51177	0.53661				
		0.65782	0.67387	0.68017	0.67815	0.66463				

Table B.1 (Continued)

α	$\beta = -0.5$	$\beta = -0.4$	$\beta = -0.3$	$\beta = -0.2$	$\beta = -0.1$	$\beta = 0$	$\beta = 0.1$	$\beta = 0.2$	$\beta = 0.3$	$\beta = 0.4$	$\beta = 0.5$
0.8						0.50859	0.50000	0.50807	0.54432	0.57058	
						0.60911	0.62109	0.61781	0.58807	$\pm 0.064553i$	
0.9						0.50428	0.50415	0.53282	0.53465	0.53714	
						0.55677	0.55881	$\pm 0.033989i$	$\pm 0.07208i$	$\pm 0.10845i$	
1						<u>0.50000</u>	0.50000	0.50000	0.50000	0.50000	0.50000
							$\pm 0.031938i$	$\pm 0.064532i$	$\pm 0.098523i$	$\pm 0.13485i$	$\pm 0.17485i$

Appendix C. Experimental results of single lap joint

In Appendix C, the experimental results considered in this paper are presented. The testing method to evaluate the adhesive strength of single lap joint is prescribed by Japanese Industrial Standards (JIS) [JIS K6850 (1999)]. However, since JIS specimen has a small thickness, it is difficult to calculate the critical stress intensity accurately because of large deformation appearing (see Fig. C.1) before debonding was not indicated in the previous studies. In this study, therefore, the thick specimens used by Park [Park *et al.* (2010)] in Fig.2 are analyzed where the adherends aluminum alloy 6061-T6 are bonded with adhesive FM73M epoxy. In this experiment, the authors prepared for the specimen very carefully to exclude the defect and voids. The aluminum surface was polished with 40 mesh sandpaper and corroded using 27% sulfuric acid and 135g/L ferric sulfate for 12min. After the corrosion step, the surfaces were cleaned using water and then dried. The assembled adhesive joints were cured by autoclaving at 120 °C for 120 min. The typical force-displacement curves of the adhesive joints show nearly linear behavior. Five specimens were tested for each case to obtain an average failure load. A drop in load was used to detect a failure. In this experiment, during the bonding process, it was found that a small void may appear in the thicker adhesive ($t_{ad} = 0.3, 0.45, 0.9\text{mm}$), which resulting in lower failure strength. To remove the voids from the thicker adhesive, the appropriate guide blocks were machined and secured onto the adhesive joints. Failure load in the specimens without internal voids were 40.5% and 46.2% larger than for those with internal voids when the adhesive lengths are 25mm and 30mm, respectively [Park *et al.* (2010)]. Usually, the internal residual stress is caused by the contraction during the curing process, which affects the adhesive strength significantly. In this experiment, it was conjectured that the adhesive protrusion may be prevented between the adherend by using the guide blocks, which results in relieving the contraction due to the curing. Therefore, the guide blocks may contribute relieving the internal stress as well as removing the voids by curing the contraction.

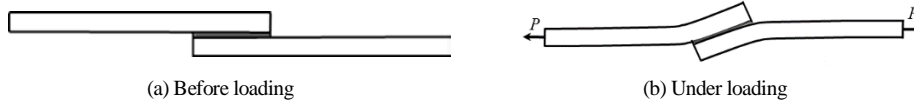


Fig. C.1. Schematic illustration of deformation of lap joint.

Table C.1 and Fig. C.2 show the fracture load P_{af} and tensile adhesive strength σ_c ($\sigma_c = P_{af} / Wt$). Fig. C3 shows the load-displacement curve of the specimens with $t_{ad} = 0.15\text{mm}$. As for all specimens except for A10, the relation between the load and displacement is almost linear with small distribution range. Therefore, it can be considered that the fractures were caused by the unstable growth of the crack which was initiated from the corner edge. The results bring the validation of the evaluation based on the ISSF. When the adhesive length becomes long under constant adhesive thickness condition, the adhesive strength tends to increase; when the adhesive layer becomes thick under constant adhesive length, the adhesive strength does not change remarkably. The experimental observation in Fig.13(a) shows that when $l_{ad} < 15\text{mm}$ the cohesive fracture occurs and when $l_{ad} > 15\text{mm}$, the adhesive fracture occurs. Nono and Nagahiro [1986] and Rodríguez *et al.* [2012] discussed the adhesive joint strength with varying adhesive geometries. If the adhesive length l_{ad} is short enough, the yielding may occur at the entire adhesive region before the ISSF at the interface end reaches the critical value, and therefore, cohesive failure occurs instead of interface failure [Nono *et al.* (1986); Rodríguez *et al.* (2012)]. They indicated that the fracture average shear stress τ_c of the adhesive layer in lap joints is almost constant when the adhesive length is small enough. The fracture for single lap joint having smaller adhesive length may be described by the average shear stress, but the fracture of single lap joint having longer adhesive length can be described by the ISSF.

Table C.1. Experimental results

Specimen	l_{ad} [mm]	t_{ad} [mm]	P_{af} [kN]		σ_c [MPa]	
			without guide block	with guide block	without guide block	with guide block
A10	10	0.15	6.87	-	19.42	-
A15	15	0.15	10.57	-	29.88	-
A20	20	0.15	12.41	-	35.08	-
A25	25	0.15	14.17	-	40.06	-
A30	30	0.15	14.56	-	41.16	-
A35	35	0.15	16.41	-	46.39	-
A40	40	0.15	18.09	-	51.14	-
A50	50	0.15	18.22	-	51.51	-
A25-30	25	0.30	14.32	19.54	40.06	31.26
A25-45	25	0.45	14.26	20.04	39.47	32.06
A25-90	25	0.90	14.19	17.54	38.09	28.06
A30-30	30	0.30	16.91	22.85	47.30	30.47
A30-45	30	0.45	16.12	23.57	44.62	31.43
A30-90	30	0.90	15.37	21.50	41.26	28.67

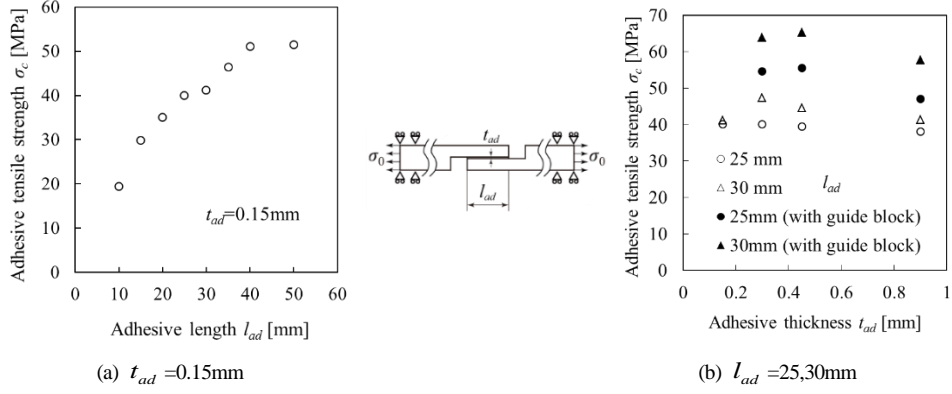
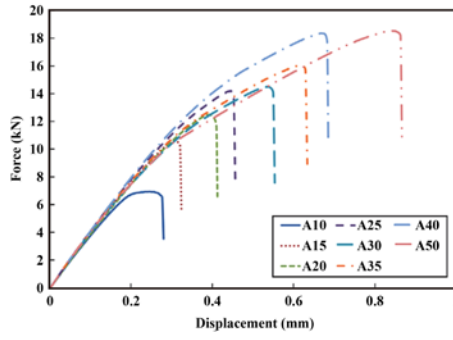


Fig. C.2. Adhesive tensile strength.


 Fig. C3 Load – displacement curves of specimens with $t_{ad} = 0.15\text{mm}$

Appendix D. Reference solutions obtained by using RWCIM

The ISSF of unknown problem for single lap joint can be obtained conveniently from the ratio as shown in Eqs. (10~12). However, since the reference solution of the ISSF is not presented in Section 3, the calculation method is presented to obtain the reference solution. The reciprocal work contour integral method (RWCIM) is based on the Betti's reciprocal theorem. By employing Williams' eigenfunction expansion method, the stress and the displacement in the vicinity of the interface corner edge are expressed as follows [Mintzas and Nowell (2012); Carpenter and Byers (1987)].

$$\sigma_{ij} = \sum_{k=1}^{\infty} K_k f_{ij}(\theta, \lambda_k) r^{\lambda_k - 1} \quad (\text{D.1})$$

$$u_i = \sum_{k=1}^{\infty} K_k g_i(\theta, \lambda_k) r^{\lambda_k} \quad (\text{D.2})$$

Here, K_k is the coefficient obtained by RWCIM, f_{ij} and g_i are the eigenfunction

related to the λ_k which depends on the angle θ . From Betti's reciprocal theorem, the following equation can be obtained [Mintzas and Nowell (2012); Carpenter and Byers (1987)].

$$\oint_C (\sigma_{ij} u_i^* - \sigma_{ij}^* u_i) n_j ds = 0 \quad (D.3)$$

Here, n_j is normal vector of the boundary C , σ_{ij}^* and u_i^* are the complementary stress and displacement that satisfy the same equilibrium and constitutive relations as σ_{ij} and u_i , respectively. The stress σ_{ij}^* and displacement u_i^* can be expressed as follows [Mintzas and Nowell (2012); Carpenter and Byers (1987)].

$$\sigma_{ij}^* = \sum_{k=1}^{\infty} K_k^* f_{ij}(\theta, \lambda_k^*) r^{\lambda_k^*-1} = \sum_{k=1}^{\infty} K_k f_{ij}(\theta, -\lambda_k) r^{-\lambda_k-1} \quad (D.4)$$

$$u_i^* = \sum_{k=1}^{\infty} K_k^* g_i(\theta, \lambda_k^*) r^{\lambda_k^*} = \sum_{k=1}^{\infty} K_k g_i(\theta, -\lambda_k) r^{-\lambda_k} \quad (D.5)$$

The integral path $C (= C_1 + C_2 + C_3 + C_4 + C_5 + C_6 + C_\varepsilon)$ is set as shown in Fig. 8. Because the lines C_1 and C_6 lie along the stress free surface, the integrals along these lines are zero. Therefore, Eq. (D.3) can be written as follows.

$$\int_{-\pi/2}^{\pi} (\sigma_{ij} u_i^* - \sigma_{ij}^* u_i) \varepsilon n_j d\theta = \int_C (\sigma_{ij} u_i^* - \sigma_{ij}^* u_i) n_j ds \quad (D.6)$$

Here, $C' = C_2 + C_3 + C_4 + C_5$. The terms of σ_{ij} and u_i in the left hand side can be expressed as Eqs. (D.1) and (D.2). The complementary stress and displacement calculated by FEM, $\sigma_{ij, FEM}$ and $u_{i, FEM}$ are substituted into the terms of σ_{ij} and u_i in the right hand side. Then, σ_{ij}^* and u_i^* are given by Eqs. (D.4) and (D.5), respectively. When $\varepsilon \rightarrow 0$, the integral in the left hand side becomes constant. The following equation is used as K_k^* [Mintzas and Nowell (2012); Carpenter and Byers (1987)].

$$1/K_k^* = \int_{-\pi/2}^{\pi} [f_{ij}(\theta, \lambda_k) g_i^*(\theta, \lambda_k^*) - f_{ij}^*(\theta, \lambda_k^*) g_i(\theta, \lambda_k)] n_j d\theta \quad (D.7)$$

The ISSF K_k can be obtained from the following equation.

$$K_k = \int_C (\sigma_{ij, FEM} u_{ik}^* - \sigma_{ijk}^* u_{i, FEM}) n_j ds \quad (D.8)$$

Here, $\sigma_{iik}^* = K_k^* f_{ii}(\theta, \lambda_k) r^{\lambda_k^*-1}$, $u_{ik}^* = K_k^* g_i(\theta, \lambda_k) r^{\lambda_k^*}$. RWCIM is useful for determining the ISSF. However, the complex and time-consuming calculations such as matrix operation and numerical integration are required, which may bring low practicality of RWCIM. Because the proposed method in Section 3 enables us to analyze the ISSF as accurately as RWCIM, the proposed method is more convenient and practical by only focusing on the FEM results at the corner point without taking risks of miscalculations.

References

- ASTM D 1002-1, “Standard test method for apparent shear strength of single-lap-joint adhesively bonded metal specimens by tension loading (metal-to-metal)”, ASTM Standards, 1-5.
- Barnes, T. A. and Pashby, I. R. (2000). Joining techniques for aluminium spaceframes used in automobiles: Part II — adhesive bonding and mechanical fasteners. *J Mater Process Tech*, **99**(1-3): 72-79.
- Bogy, D.B. (1968). Edge-bonded dissimilar orthogonal elastic wedges under normal and shear loading, *Trans ASME J Appl Mech*, **35**: 460-466.
- Bogy, D.B. (1971). Two edge-bonded elastic wedges of different materials and wedge angles under surface tractions, *Trans ASME J Appl Mech*, **38**: 377-386.
- BS EN 1465:1995, “Adhesives-determination of tensile lap-shear strength of rigid-to-rigid bonded assemblies”.
- Carpenter, W. C. and Byers, C. (1987). A path independent integral for computing stress intensities for V-notched cracks in a bi-material, *Int J Fract*, **35**: 245-268.
- Cheng, H. C., Huang, H. H., Chen, W. H. and Lu, S. T. (2015). Hygro-thermo-mechanical behavior of adhesive-based flexible chip-on-flex packaging. *J Electron Mater*, **44**(4):1220-1237.
- Dundurs, J. (1969). Discussion: “Edge-bonded dissimilar orthogonal elastic wedges under normal and shear loading”. *ASME J Appl Mech*, **36**: 650-652.
- Gautam, S.S. and Sauer, R.A. (2014). A composite time integration scheme for dynamic adhesion and its application to gecko spatula peeling, *Int. J. Comput. Methods*, **11**(5): 1350104
- Hattori, T., Sakata, S., Hatsuda, T. and Murakami, G. (1988). A stress singularity parameter approach for evaluating adhesive strength. *JSME Int J Ser 1 Solid Mech Strength Mater*, **31**(4):718–23.
- Hirakata, H., Takahashi, Y., Matsumoto, S., Kitamura, T. (2006). Dominant stress region for crack initiation at interface edge of microdot on a substrate. *Eng Frac Mech*, **73**: 2698-2709.
- JIS K6850:1999. Adhesives-Determination of tensile lap-shear strength of rigid-to-rigid bonded assemblies.
- Labossiere, P. E. W., Dunn, M. L., Cunningham, S. J. (2002). Application of bimaterial interface corner failure mechanics to silicon/glass anodic bonds. *Journal of the Mechanics and Physics of Solids*, **50**(3): 405-433.
- Khan, M.A., El-Rimawi, J. and Silberschmidt, V.V. (2017). Numerical representation of multiple premature failures in steel-plated RC beams, *Int. J. Comput. Methods*, **14**(4): 1750035
- Kitamura, T., Shibutan, T. and Ueno, T. (2002). Crack initiation at free edge of interface between thin films in advanced LSI. *Eng Frac Mech*, **69**: 1289-1299.
- Kyogoku, H., Sugibayashi, T. and Ikegami, K. (1986). Strength evaluation of asymmetric single lap joints: 3rd Report, Effects of mechanical properties of adherends. *Bull JSME*, **29**(258): 4064-4071.
- Mintzas, A. and Nowell, D. (2012). Validation of an H_{cr} -based fracture initiation criterion for adhesively bonded joints. *Eng Fract Mech*, **80**: 13-27.
- Miyazaki, T., Noda, N. A., Ren, F., Wang, Z., Sano, Y., Iida, K. (2017). Analysis of intensity of singular stress field for bonded cylinder and bonded pipe in comparison with bonded plate. *Int J Adhes Adhes*, **77**: 118-137.
- Noda, N.A., Chen, X, Sano, Y., Wahab, M.A., Maruyama, H., Fujisawa, R. (2016). Effect of pitch difference between the bolt–nut connections upon the anti-loosening performance and fatigue life. *Materials & Design*, **96**: 476-489.
- Noda, N.A., Suryadi, D., Kumasaki, S., Sano, Y., Takase, Y. (2015a) Failure analysis for coming out of shaft from shrink-fitted ceramic sleeve. *Engineering Failure Analysis*, **57**: 219-235.
- Noda, N.A., Miyazaki, T. and Li, R., Uchikoba, T. and Sano, Y. (2015b). Debonding strength evaluation in terms of the intensity of singular stress at the interface corner with and without fictitious crack. *Int J Adhes Adhes*, **61**: 46-64.

- Noda, N. A., Uchikoba, T., Ueno, M., Sano, Y., Iida, K., Wang, Z., Wang, G. (2015c). Convenient Debonding Strength Evaluation for Spray Coating Based on Intensity of Singular Stress. *ISIJ International*, **55**(12): 2624-2630.
- Noda, N.A., Shen, Y., Takaki, R., Akagi, D., Ikeda, T., Sano, Y., Yasushi Takase Y. (2017). Relationship between strain rate concentration factor and stress concentration factor. *Theoretical and Applied Fracture Mechanics*, **90**: 218–227.
- Noda, N. A., Shirao, R. and Li, J. (2007). Sugimoto JS. Intensity of singular stress fields causing interfacial debonding at the end of a fiber under pullout force and transverse tension. *Int J Solids Struct*, **44**:4472–91.
- Noda, N. A. Takase Y (2003). Generalized stress intensity factors of V-shaped notch in a round bar under torsion, tension, and bending. *Eng Fract Mech*, **70**: 1447-1466.
- Nono, K. and Nagahiro, T. (1986). A comparison of predicted strength and experimental results of adhesive joints. *Trans Jpn Soc Mech Eng A*, **52**(479): 1698-1707 (in Japanese).
- Park, J. H., Choi, J. H. and Kweon, J. H. (2010). Evaluating the strengths of thick aluminum -to-aluminum joints with different adhesive lengths and thicknesses, *Compos Struct*, **92**: 2226-2235.
- Pathak, P., Zhang, Y.X. and Teng, X. (2017). Nonlinear finite element analysis of FRP strengthened RC beams with Bond-Slip effect, *Int. J. Comput. Methods*, **14**(3): 1750032
- Qian, Z. and Akisanya, A. R. (1998). An experimental investigation of failure initiation in bonded joints, *Acta Mater*, **46**(14): 4895-4904.
- Reedy Jr E. D. and Guess, T. R. (1993). Comparison of butt tensile strength data with interface corner stress intensity factor prediction. *Int J Solids Struct*, **30**(21): 2929-2936.
- Rodríguez, R. Q. , Paiva, W. P. , Sollero, P., Rodrigues, M. B. , Albuquerque, E. L. (2012), Failure criteria for adhesively bonded joints, *Int J Adhes Adhes*, **37**: 26-36.
- Shibutani, T., Tsuruga, T., Yu, Q. and Shiratori, M. (2003). Criteria of crack initiation at edge of interface between thin films in opening an sliding modes for an advanced LSI. *Trans Jpn Soc Mech Eng A*, **69**(685): 1368-1373 (in Japanese).
- Shibutani, T. (2004). Evaluation of crack initiation at interfacial edge on the basis of fracture mechanics concept and application to electronics devices. *J Jpn Inst Electron Packag*, **7**(7): 639-644 (in Japanese).
- Shiratori, M. (1994). Problems of joints in packaging of electronic devices. *Trans Jpn Soc Mech Eng A*, **60**(577): 1905-1912 (in Japanese).
- Suzuki, Y. (1987). Adhesive tensile strengths of scarf and butt joints of steel plates (Relation between adhesive layer thicknesses and adhesive strengths of joints). *JSME IntJ*, **30**(265):1042–51.
- Takahashi, Y., Aihara, K., Ashida, I., Niguchi, K., Yamamoto, Y., Arai, S., Muto, S., Tanaka, N. (2016). Evaluation of interfacial fracture strength in micro-components with different free-edge shape. *Mechanical Engineering Journal*. DOI: 10.1299/mej.16-00108.
- Treifi, M. and Oyadiji, S. O. (2013). Evaluation of mode III stress intensity factors for bi-material notched bodies using the fractal-like finite element method. *Comput Struct*, **129**: 99-110.
- Wang, Z., Noda, N. A., Ueno, M, Sano, Y. (2016). Optimum Design of Ceramic Spray Coating Evaluated in Terms of Intensity of Singular Stress Field. *steel research international*, **88**(7): DOI: 10.1002/srin.201600353.
- Yuuki, R. (1993). Mechanics of interface. *Baifuukann*, Tokyo, 283p (in Japanese).
- Zhang, Y., Noda, N. A., Takaishi, K. and Lan, X. (2010). Effect of adhesive thickness on the intensity of singular stress at the adhesive dissimilar joint. *J Solid Mech Mater Eng*, **4**(10):1467–79.
- Zhang, Y., Noda, N. A., Wu, P. Z. and Duan, M. L. (2015). A mesh-independent technique to evaluate stress singularities in adhesive joints. *Int J Adhes Adhes*, **57**:105–117; Zhang, Y., Noda, N. A., Wu, P. Z. and Duan, M. L. (2015). The corrigendum to a mesh-independent technique to evaluate stress singularities in adhesive joint. *Int J Adhes Adhes*, **60**:130.